Full length article

On the role of boron on improving ductility in a new polycrystalline superalloy

Paraskevas Kontis [a], Enrique Alabort [b], Daniel Barba [b], David M. Collins [a], Angus J. Wilkinson [a], Roger C. Reed [a, *]

[a] *Department of Materials, University of Oxford, Parks Road, Oxford OX1 3PH, UK*
[b] *Department of Engineering Science, University of Oxford, Parks Road, Oxford OX1 3PJ, UK*

ARTICLE INFO

ABSTRACT

The role of boron in promoting ductility at high temperature in a prototype nickel-based superalloy designed for industrial gas turbines is studied. Both a boron-containing and boron-free variant are tested in tension at 750 °C, with further *in-situ* tests carried out using scanning electron microscopy (SEM), to clarify the mechanism of ductility improvement. The improvement in ductility is observed to be greater at the lowest investigated strain rate, where the grain boundary character plays a significant role on the mechanical properties; no ductility improvement was observed at the highest investigated strain rate. The *in-situ* tests were also performed at 750 °C and revealed directly the greater susceptibility of the grain boundary morphology in the boron-free case to fracture and − in the boron-containing case − the mechanism of ductility enhancement. The findings are supported further by high-resolution electron backscattered diffraction (HR-EBSD) strain mapping which confirms that the distribution of elastic strain and geometrically necessary dislocation (GND) content are influenced markedly by boron addition. The mechanism through which boron indirectly enhances the mechanical properties at elevated temperatures is discussed.

1. Introduction

The ductility of the nickel-based superalloys can be exploited for high temperature applications [1]. But what factors influence it? When in polycrystalline form, intergranular fracture is common particularly under the high temperature conditions of greatest technological relevance; it follows that the effects occurring at the grain boundaries must play a significant role in promoting − or limiting − ductility [2,3]. But more fundamental studies are needed to elucidate the physical mechanisms which are at play.

One difficulty is that traditional approaches rely upon post-mortem studies for the deduction of microstructure/property relationships in such materials. For example, emphasis is often placed on fracture surfaces or dislocation structures examined at ambient conditions, when in fact it is the effects occurring at temperature and with the load applied which are clearly of the greatest relevance. *In-situ* studies circumvent these difficulties and are therefore of significant value in the search for a greater appreciation of the phenomena which control properties [4,5].

In this paper, a study is made of the behaviour of a prototype polycrystalline superalloy designed recently for power generation applications. A boron-free and a boron-containing variant are tested in tension at different strain rates and at elevated temperatures. *In-situ* tensile experiments are also carried out in a scanning electron microscope at elevated temperatures to examine the factors promoting ductility. High-resolution electron backscatter diffraction (HR-EBSD) measurements are made at interrupted intervals of tensile deformation, thus enabling a cross-correlation based strain mapping method to be undertaken. In this way, insights are provided into the role played by boron in promoting ductility in these alloys.

2. Background

As will become apparent later in this paper, a significant role is played by boron in the serration of grain boundaries in this superalloy. Therefore attention is paid here to the prior literature on

* Corresponding author.
   E-mail address: roger.reed@eng.ox.ac.uk (R.C. Reed).

this topic. The serration of grain boundaries has been reported to have an influence on mechanical properties in polycrystalline nickel-based superalloys by impeding grain crack propagation [6–8]. In particular, voids and cavities forming at serrated grain boundaries are often assumed not to easily interlink and this prevents the formation of a continuous crack path [9,10]. Moreover, serrated grain boundaries invoke longer diffusion paths along grain boundaries [11]. Environmental effects at elevated temperatures are thus retarded. Whilst some theories exist on the exact formation mechanism, a consensus on the formation of grain boundary serrations remains absent. Furthermore, the definition of whether a grain boundary is serrated is currently rather arbitrary; for example, a boundary may be considered serrated when its 'amplitude' is larger than 0.5 μm [6].

Different theories have been developed that attempt to rationalise the formation of serrated grain boundaries in nickel superalloys. Serrated grain boundaries are often strongly associated with heterogeneous nucleation of γ' in their vicinity [10,12]. In this case, a serration results from the pinning of a grain boundary at a primary γ' precipitate in conjunction with its movement between the primary γ' particles [13]. The grain boundary migration continues until γ' particles form homogeneously throughout the grain − thus forming a physical barrier that prevents further migration. Moreover, it is well established that the occurrence of a serration depends strongly on the cooling rate from the solution treatment temperature through the γ' precipitation zone [11,13–15]. Low cooling rates result in serrated grain boundaries, since there is then sufficient time for grain boundaries to grow. Rapid cooling leads to smaller heterogeneously formed γ' particles; consequently planar grain boundaries form [11,14]. The serration amplitude and wavelength increase as cooling rate decreases and solution temperature increases [16,17]. For formation of serrated grain boundaries, it is also often thought that the solution heat treatment temperature should be well above the solvus of the major grain boundary carbides, e.g. $M_{23}C_6$, [10]. That way the carbides are dissolved and the grain boundary can move in the absence of obstacles. By contrast, different studies have postulated that serrated grain boundaries form in the presence of $M_{23}C_6$ carbides at the grain boundaries, whereas planar grain boundaries occur in their absence [18].

It has also been suggested [6] that alloy composition plays a role − for instance by providing a driving force for grain boundary serrations from discontinuous chromium and carbon segregation along the grain boundaries. Inhomogenous segregation of carbon and chromium are expected to provide varying magnitudes of lattice distortion along the grain boundaries, while this is not observed when the segregation is continuous. This has been rationalised using a calculation by McLean [19], where the lattice strain energy for carbon, given as 48 kJ mol^{-1}, was reported to be far greater than chromium, at 1.2 kJ mol^{-1} [6]. As a consequence, grain boundary serrations are not expected in cases of low carbon content in solid solution. If the accumulation of strain energy results in a distortion of the grain boundary itself, one can infer that serrated grain boundaries may occur due to discontinuous segregation. It was suggested that the non-uniform distortional lattice strain along the grain boundary acts as the driving force for the onset of grain boundary serrations. Contrary to this, in a study of a ternary Ni-xCr-0.1C model alloy, chromium was found to increase the serration amplitude [20].

In addition to carbon and chromium, boron has also been found to segregate to serrated grain boundaries in Astroloy, as confirmed by atom probe studies [21]. Here, serrated grain boundaries were observed in a boron-containing alloy, but planar grain boundaries occur in the absence of boron.

3. Experimental procedures

3.1. Materials

The prototype nickel-based polycrystalline superalloy STAL15-CC investigated in this study has a composition shown in Table 1 and grain size of ~750 μm. The chemical analysis was conducted in an independent laboratory where the carbon content was measured using a LECO CS444 analyser and for the other elements the inductively coupled plasma OES (ICP-OES) method was utilised. To investigate the effect of boron, test-bars with no boron (boron free − BF) and boron-containing (BC − 0.05 at.% B) content were produced by conventional casting (CC). Castings in the form of tapered rods were prepared at Doncasters Precision Castings Ltd., using casting stock melted by Ross & Catherall (Sheffield, United Kingdom). After conventional casting, a hot isostatic press (HIP) was used to consolidate the as-cast bars, in order to eliminate microporosity and improve mechanical properties. The HIP process was performed at 1195 °C for 5 h under 175 MPa pressure. The process of HIP was followed by a stage of primary ageing at 1120 °C for 4 h and a subsequent second stage of ageing at 845 °C for 24 h, both followed by air-cooling. Note that the same heat treatment conditions were applied to both alloys.

3.2. Mechanical tests at elevated temperature

Tensile tests were performed using an Instron 8800 electro-thermal mechanical testing (ETMT) device at 750 °C under displacement control with speed of 10 μm s^{-1} and 0.1 μm s^{-1}, corresponding to strain rates, $\dot{\varepsilon}$, of approximately 2×10^{-3} s^{-1} and 2×10^{-5} s^{-1}, respectively. Specimens were machined from fully heat treated bars by electro-discharge machining (EDM). The gauge volume of the specimens was designed as 5 mm length × 2 mm width × 1 mm thick. Specimens were mechanically ground with abrasive media prior to tests to remove the oxidised layer present from the EDM. Heating was achieved by passing direct current (DC) through the gauge length of the specimen controlled by a thermocouple which was spot-welded to the centre of the gauge length. The displacement between the grips was measured with the use of a linear variable differential transducer (LVDT). Following tensile failure of the boron-free and boron-containing samples, their fracture surfaces were characterised using an optical Alicona microscope.

In-situ tensile tests were performed at 750 °C and under displacement control with speed of 0.1 μm s^{-1}, corresponding to strain rate, $\dot{\varepsilon}$, of approximately 2×10^{-5} s^{-1} to failure. A Kammrath-Weiss *in-situ* module, equipped with a resistance heater, was mounted on a Zeiss EVO SEM with a LaB$_6$ filament. Double dogbone specimens were machined from fully heat-treated bars by EDM with a gauge volume of 5 mm length × 2 mm width × 1 mm thick. Once again the surfaces were mechanically ground with abrasive media to a 1 μm finish. Secondary electron images were obtained at 750 °C with surfaces etched using Kalling's solution to reveal grain boundaries. Two thermocouples were used to monitor temperature during the tests; one was fitted between the sample and the heater and the other was spot-welded onto the sample surface. In order to

Table 1
Summary of chemical compositions of the different STAL15-CC variants investigated in this work (at.%).

Alloy	B	C	Co	Cr	Mo	W	Al	Ta	Hf
Boron-free	<0.005	0.44	5.50	16.45	0.61	1.26	10.00	2.41	0.02
Boron-containing	0.05	0.47	5.50	16.55	0.59	1.26	10.09	2.40	0.02

improve thermal conductivity in vacuum conditions, heating was via conduction from a heated surface, with the sample held in place with tungsten wire springs; gold leaves were placed in between to improve thermal conductivity. The displacement between the grips was measured with the use of an LVDT. An illustration of the experimental set-up is shown in Fig. 1. Subsurface characterisation of the deformed specimens was conducted using a Zeiss NVision 40 dual column FIB. Sections were milled normal to the sample surface and areas of interest were imaged with secondary electrons. The oxidation behaviour of the MC carbides was also considered in this study. For this purpose, flat polished specimens to 1 μm finish were exposed at 750 °C for 50 h in air.

3.3. High-resolution EBSD strain mapping

In-situ tensile specimens were characterised by cross-correlation-based high-resolution electron backscattered diffraction (HR-EBSD) before and after deformation at elevated temperatures. This method allows the investigation of elastic strains at microscopic scales [22]. Information on plastic deformation can be inferred by quantifying the geometrically necessary dislocation (GND) density, based upon measurement of the lattice curvature and subsequent analysis of the Nye tensor [23]. This technique has been utilised in various materials to study for instance the GND distributions after tensile deformation in Ti [24] and residual stresses and GND accumulation in annealed [25,26] and deformed copper [27], for example. The method has also been applied to superalloys with measurements being made of strains and GND densities near carbide particles and oxide agglomerates after thermal loading and room temperature deformation [28,29].

The specimens were polished to a 0.04 μm colloidal silica finish
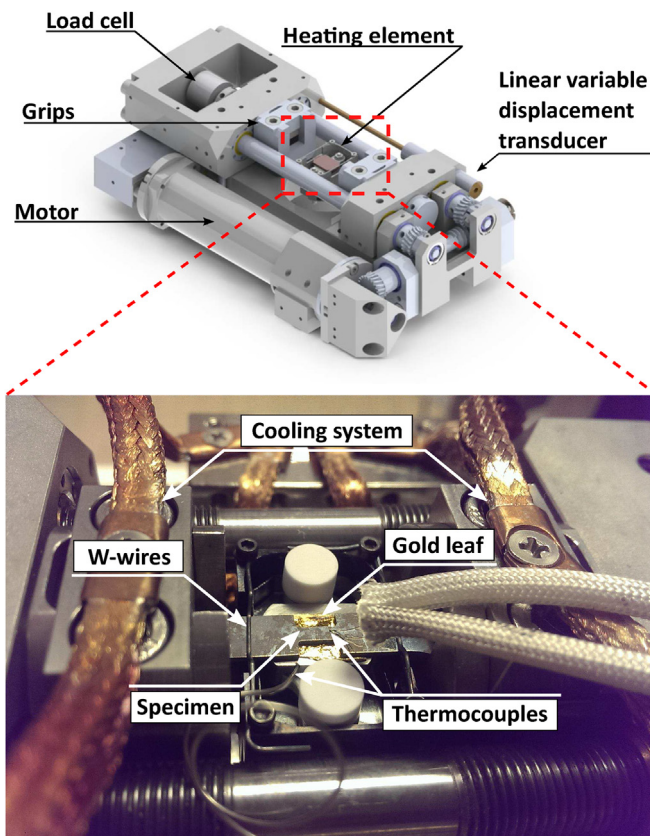

Fig. 1. Experimental set-up for the *in-situ* tensile tests at 750 °C.

and grain boundaries perpendicular to the tensile axis were selected. Prior to any deformation, backscattered images were taken and HR-EBSD maps were collected on a JEOL 6500F. The specimens were then deformed under vacuum at 750 °C and under displacement control with speed of 0.1 μm s^{-1} using the *in-situ* tensile module and interrupted after a total of 0.5% permanent deformation. In order to minimise residual thermal stresses during the cooling, the specimens were then cooled slowly (0.8 °C/s) to room temperature and diffraction patterns were collected on the JEOL 6500F. HR-EBSD maps were subsequently collected from the same grain boundary regions as prior to deformation. The HR-EBSD analysis was performed on a different microscope than the one used for the *in-situ* tensile tests, primarily due to long time required for the diffraction patterns collection. HR-EBSD patterns were recorded using a 1000 × 1000 pixel, peltier cooled charge coupled device (CCD) camera at full resolution. The scintillator screen was held at a capture angle of 70° to the sample surface. The SEM conditions used were 20 keV beam energy, and a beam current of ~14 nA, for which exposure time was about 0.5 s. All maps were obtained using a 50 nm step size, 20 regions of interest (ROI) and remapping. The elastic constants of nickel was used for the γ/γ' microstructure [30]. The elastic constants of the MC carbides are not known therefore some of the strain map figures consist of blank regions. The amplitude, A, and the wavelength, λ, of serrated grain boundaries were measured using the ImageJ software and the misorientation between the grains was calculated using the OIM data analysis software.

4. Results

### 4.1. Characterisation of virgin microstructure prior to deformation

Figs. 2(a) and 3(a) show backscattered SEM images from typical fully heat treated grain boundary regions of both investigated alloys. Corresponding EBSD analysis is shown in Figs. 2(b) and 3(b). The inverse pole figure (IPF) maps are shown to identify the crystal direction along the loading axis and strain maps associated with ε_{11}, ε_{12} and ε_{22} components are given. Lattice rotations and elastic strains within the sample cause small shifts in the positions of zone axes and other features in the EBSD patterns obtained as the electron beam is scanned over the sample. These small pattern shifts are measured using automated image-processing based on cross-correlation analysis and then related to the size and nature of the strains and rotations.

Serration of the grain boundary is present in the case of the boron-containing alloy, whereas a relatively planar grain boundary is observed in the boron-free sample. In a previous study, a systematic characterisation of the grain boundary phases using high-resolution characterisation methods, such as atom probe tomography and Nano-SIMS was carried out [3]. It was shown that in the case of the boron-free alloy Cr-rich $M_{23}C_6$ were found to decorate the grain boundaries whereas their formation was suppressed by the addition of boron. Instead, Cr-rich M_5B_3 borides form along the grain boundaries of the boron-containing alloy. The precipitation of Ta-rich MC carbides was not influenced by the addition of boron. A TEM micrograph from the boron-containing alloy showing intergranular M_5B_3 borides is given in Fig. 4. In addition, the secondary γ' particles at the grain boundaries exhibit a different morphology and shape between the boron-free and boron-containing alloys. In the case of the boron-containing alloy, γ' layers formed at the grain boundaries with their diameter larger than secondary particles within the grains. By contrast, no γ' envelopes were observed to form in the boron-free alloy. The formation of the grain boundary γ' layers is further discussed in the subsequent section.

The γ/γ' microstructure is revealed in the strain maps of the
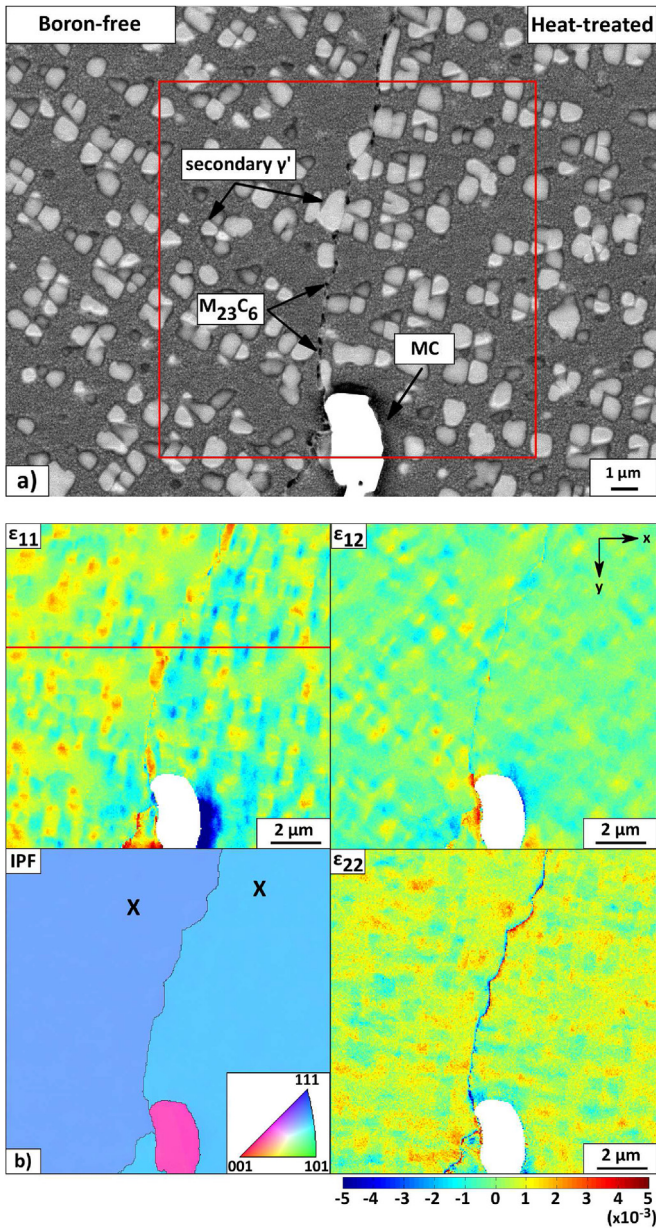
Fig. 2. Grain boundary region from the boron-free alloy: a) backscattered SEM image after full heat treatment and b) HR-EBSD strain maps alongside inverse pole figure (IPF) map of the investigated area as denoted by the red box. The red line corresponds to line-scans shown in Fig. 12. The X's indicate the reference points for the strain map analysis. (For interpretation of the references to colour in this figure legend, the reader is referred to the web version of this article.)
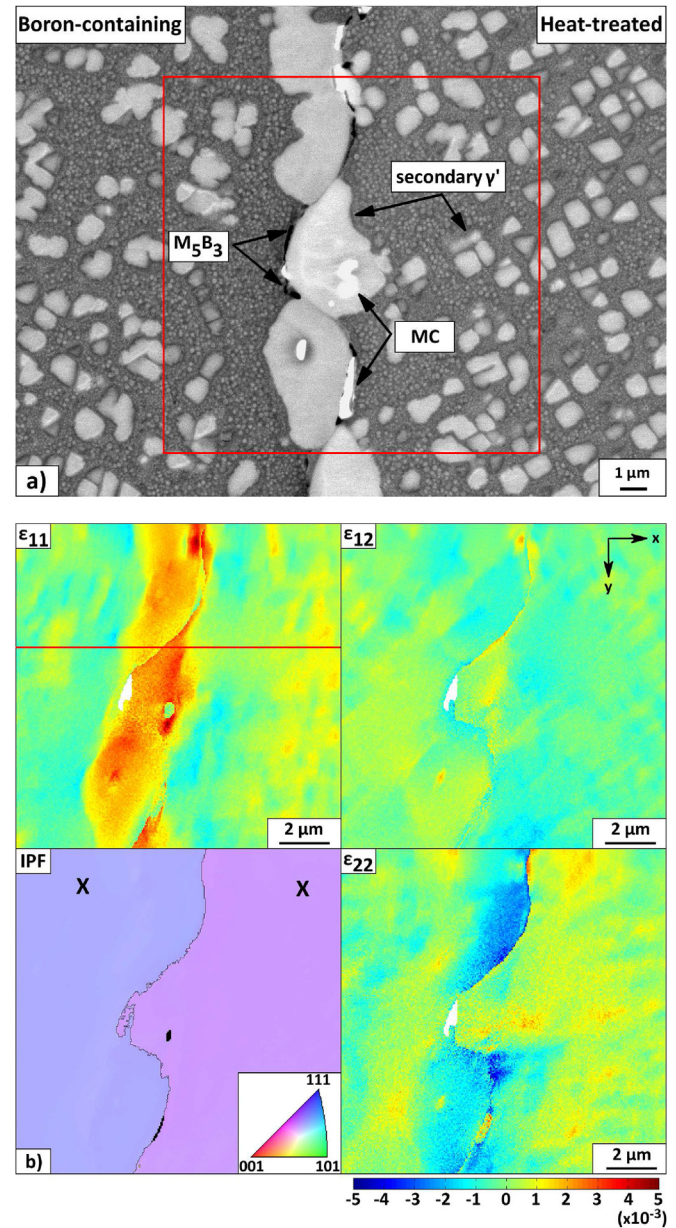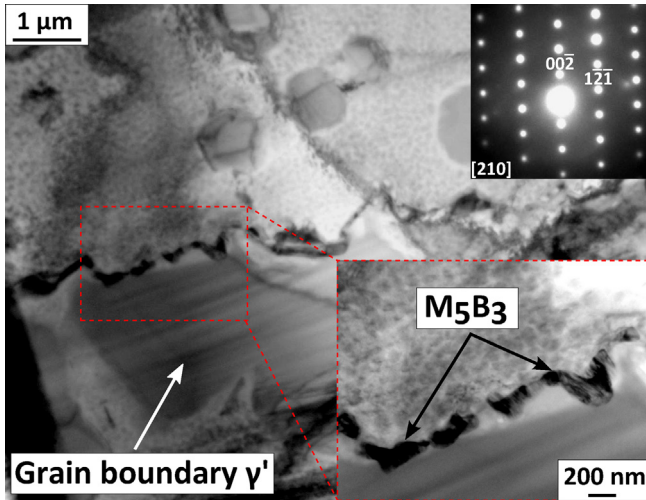
Fig. 3. Grain boundary region from the boron-containing alloy: a) backscattered SEM image after full heat treatment and b) HR-EBSD strain maps alongside inverse pole figure (IPF) map of the investigated area as denoted by the red box. The red line corresponds to line-scans shown in Fig. 12. The X's indicate the reference points for the strain map analysis. (For interpretation of the references to colour in this figure legend, the reader is referred to the web version of this article.)

samples prior to deformation as illustrated in Figs. 2(b) and 3(b). Cooling from the ageing temperature combined with the different thermal expansion coefficients between the γ/γ' microstructure and the carbides/borides results in residual thermal strains, as can be seen in the HR-EBSD maps.

In the boron-free case residual thermal strains are observed in the vicinity of MC carbide at the grain boundary. In particular, the normal strain ε_{11} along the horizontal x axis is mostly compressive to the right of the MC carbide. Similar observations were made before for a directionally solidified superalloy containing blocky MC carbides and for a powder metallurgy produced nickel superalloy containing non-metallic inclusions [28,29]. Any direct correlation of residual thermal strains with the presence of $M_{23}C_6$ carbides

along the grain boundaries was not possible, due to the small size of these particles. Thermal residual strains are uniformly distributed within the grains.

In the boron-containing alloy the intergranular MC carbides are mainly enveloped within γ' layers along the grain boundary; such layers were not observed in the boron-free alloy. The observed residual thermal strains are concentrated around and within these layers. The grain boundary γ' forms an almost continuous layer along this part of the boundary and thermal strains ε_{11} across the vertical boundary layer are more tensile within that layer. The strains ε_{22} along the layer tend to be compressive within the grain boundary γ'. Strain variations associated with the γ' particles within the grain are present but less obvious in the boron-

Fig. 4. TEM micrograph of fully heat treated microstructure from a grain boundary region of the boron-containing alloy. A representative M_5B_3 along the grain boundary and grain boundary γ' are illustrated. Selected area diffraction pattern collected from the borides is shown along the [210] direction.

containing alloy due to the presence of the grain boundary γ'. It is noted that this occurs at a grain boundary which is serrated. Variations in the residual thermal strains across the grains can be observed in the boron-containing case.

4.2. Tensile performance at 750 °C

The representative stress *vs.* engineering strain curves for both boron-free (BF) and boron-containing (BC) alloys at 750 °C and strain rates, $\dot{\varepsilon}$, 2×10^{-3} s^{-1} and 2×10^{-5} s^{-1} are shown in Fig. 5. It can be seen that the beneficial effect of boron at elevated temperatures results in a strain rate dependent character. For the higher investigated strain rate two tests were performed for each alloy and representative data are given in Fig. 5. It can be seen that the performance of both alloys is similar in terms of ductility − implying no improvement in tensile properties by the addition of boron.

However, as the strain rate decreases, a different behaviour is
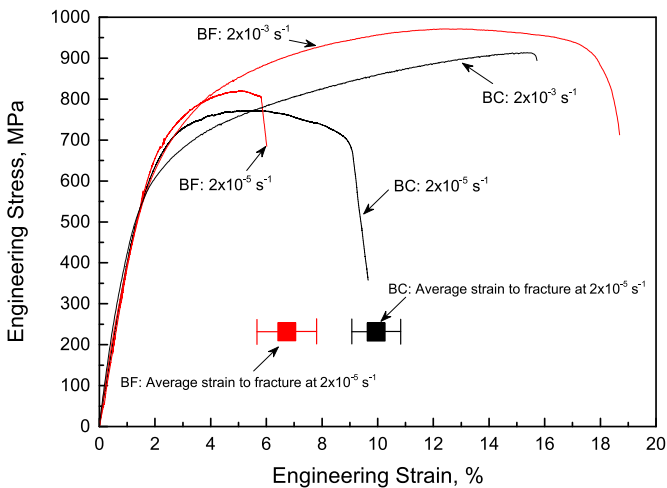
Fig. 5. Engineering stress *vs.* engineering strain curves at 750 °C and strain rates 2×10^{-3} s^{-1} and 2×10^{-5} s^{-1} for both boron-free (BF) and boron-containing (BC) alloys collected using the ETMT machine. Note the average strain to fracture from three tests for the 2×10^{-5} s^{-1} strain rate. Error bars correspond to the standard deviation of the measurements.

observed for both alloys. In the case of the boron-free alloy, a dramatic drop compared to the higher rate test by nearly 60% in ductility is observed, whereas in the boron-containing alloy the ductility is reduced by only 30%. In order to make sure that the decrease in ductility is not related to grain size and orientation effects, three tests were performed at this condition for each material. The difference in average strain to fracture is illustrated in Fig. 5, where the error bars correspond to the standard deviation of the measurements. At the lower strain rate, diffusional phenomena at grain boundaries becomes more important. Thus, factors such as the grain boundary character − and therefore boron addition − become highly important. For this reason, the *in-situ* tensile tests were performed only at the lower investigated strain rate.

The improvement in ductility is also confirmed by the examination of the different fracture surface character between the boron-free and boron-containing alloy. Fig. 6 illustrates surface measurements of the fracture surfaces of the specimens tested using the ETMT at strain rate 2×10^{-5} s^{-1}. In the boron-free case shown in Fig. 6(a), a relatively flat fracture surface is observed, indicating a rather brittle fracture of the boron-free alloy at 750 °C. By contrast, a less flat fracture surface is observed in the case of the boron-containing alloy (Fig. 6(b)), implying greater ductility.

4.3. In-situ observations

Interrupted *in-situ* tensile tests were performed for both alloys, investigating the grain boundaries shown in Figs. 2(a) and 3(a). The tensile tests were performed at 750 °C and under displacement control with speed of 0.1 μm s^{-1}, corresponding to strain rate, $\dot{\varepsilon}$, of 2×10^{-5} s^{-1}. They were interrupted after a total of 0.5% permanent plastic deformation, in order to collect data for EBSD strain mapping analysis. Figs. 7(a) and 8(a) show the analysed grain boundary regions from the boron-free and boron-containing alloy after the
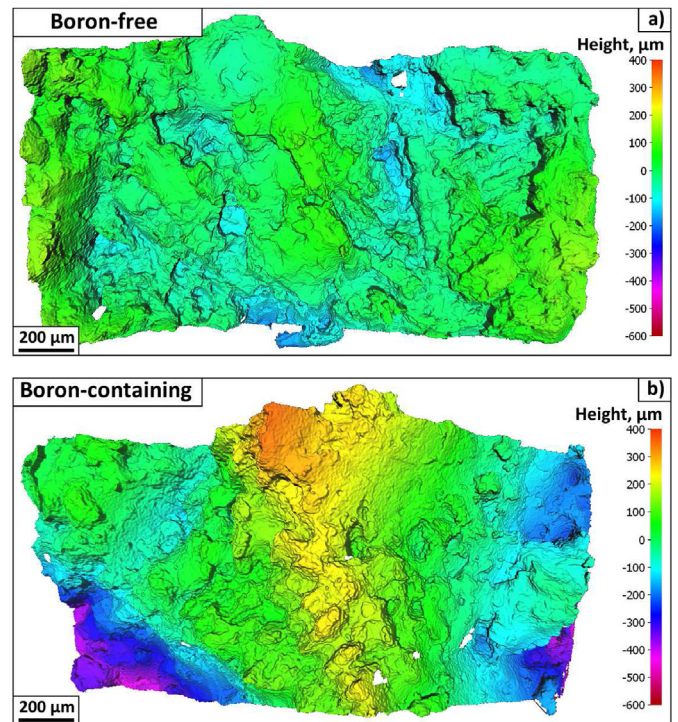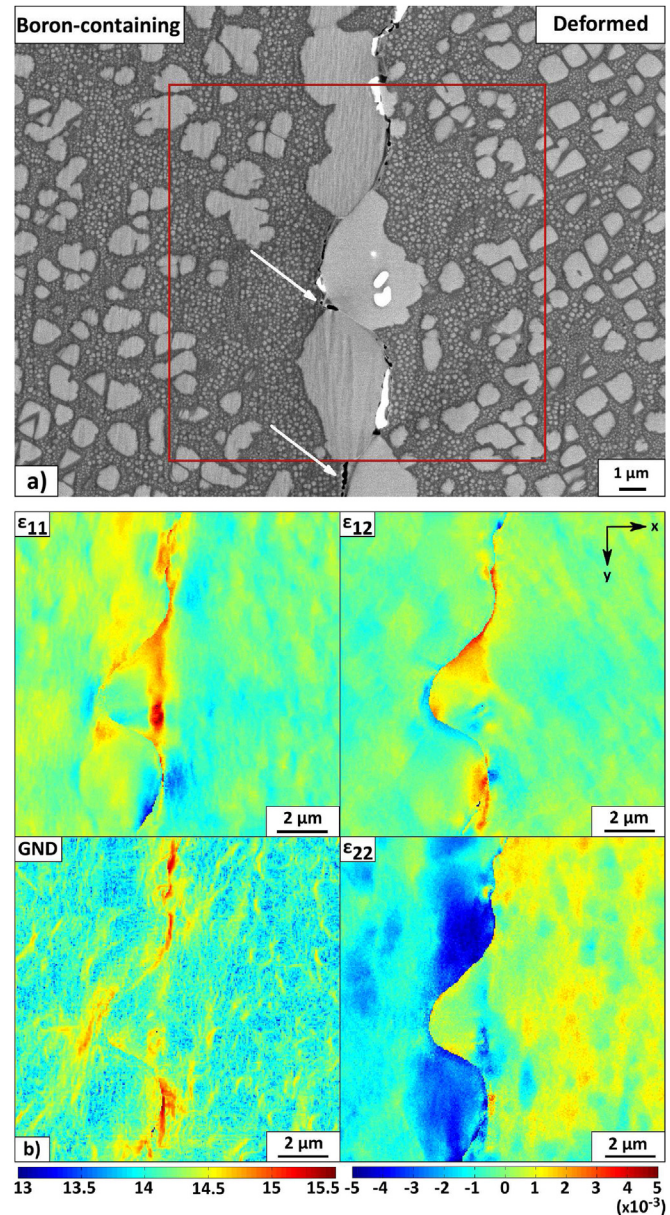

Fig. 6. Fracture surfaces of ETMT specimens from: a) boron-free and b) boron-containing alloys tested at 750 °C and strain rate 2×10^{-5} s^{-1}. Topography measurements were performed using an Alicona microscope.
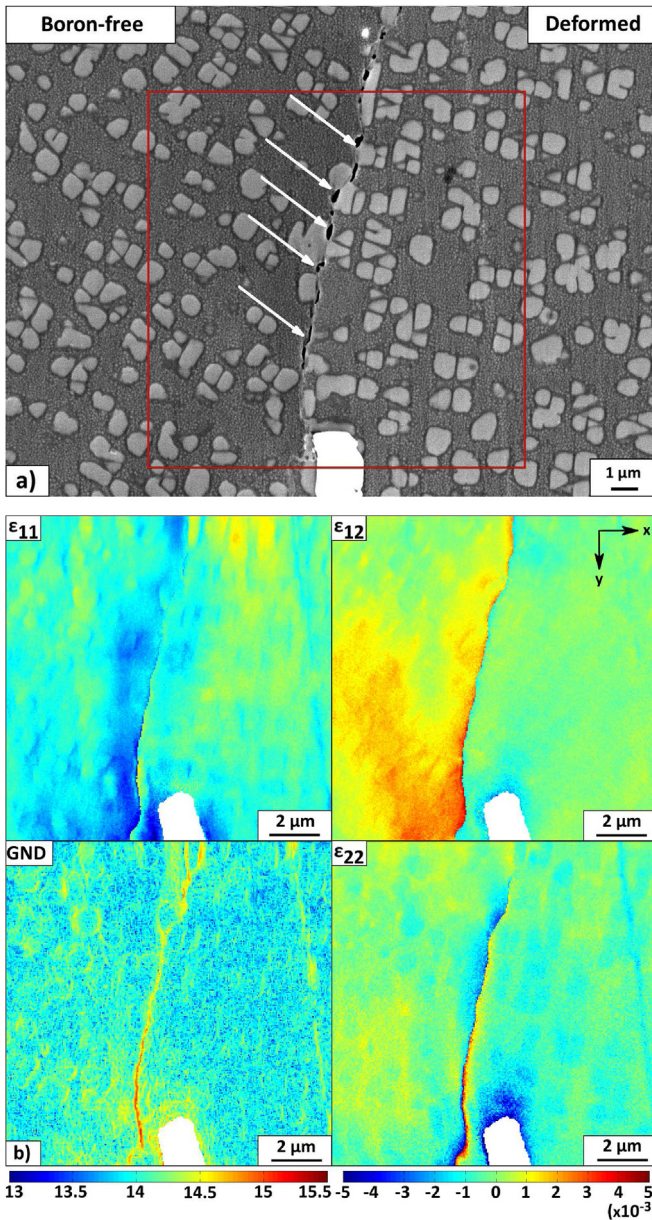
Fig. 7. Grain boundary region from the boron-free alloy: a) backscattered SEM image after ~0.5% deformation at 750 °C and strain rate 2×10^{-5} s^{-1} and b) HR-EBSD strain maps of the investigated area as denoted by the red box and GND density map after deformation with the scale bar in $\log_{10}$ scale of dislocation lines m^{-2}. Note the load direction is along the x axis. The white arrows indicate voids. (For interpretation of the references to colour in this figure legend, the reader is referred to the web version of this article.)

Fig. 8. Grain boundary region from the boron-containing alloy: a) backscattered SEM image after ~0.5% deformation at 750 °C and strain rate 2×10^{-5} s^{-1} and b) HR-EBSD strain maps of the investigated area as denoted by the red box and GND density map after deformation with the scale bar in $\log_{10}$ scale of dislocation lines m^{-2}. Note the load direction is along the x axis. The white arrows indicate voids. (For interpretation of the references to colour in this figure legend, the reader is referred to the web version of this article.)

deformation and corresponding HR-EBSD strain maps are shown in Figs. 7(b) and 8(b), respectively.

After deformation the HR-EBSD maps reveal significant differences between the two alloys. In the boron-free case, the most striking feature is the band of high in-plane shear strain ε_{12} in the left hand grain which is concentrated near the grain boundary and is particularly intense near the MC carbide towards the bottom of the map. The normal strains (ε_{11} and ε_{22}) show smaller variations compared to the shear strain and variations around the secondary γ' are less marked than before deformation. The GND density map in Fig. 7(b) shows a thin band of high GND density which accumulates along nearly the entire length of the investigated grain boundary. The GND density map also shows rings of higher density

generated by dislocation activity in the γ matrix surrounding the secondary γ' particles. Microvoids have also formed at the grain boundaries associated with $M_{23}C_6$ carbides as indicated by white arrows in Fig. 7(a).

In the case of the boron-containing alloy, the band of high ε_{11} strain across the grain boundary γ' layer has been significantly reduced by the deformation, as illustrated in Fig. 8(b). In-plane shear strains ε_{12} increase markedly compared to the undeformed state and high values are localised at the grain boundary within the grain boundary γ'. The GND density shows greater dislocation storage close to the grain boundary compared to the boron-free alloy, and furthermore the high GND regions are not continuous along the grain boundary but instead are strongly associated with
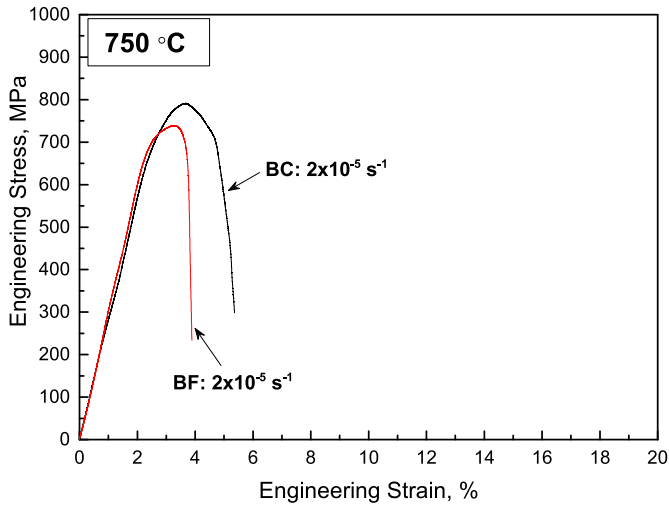
Fig. 9. Engineering stress *vs.* engineering strain curves at 750 °C and strain rate 2×10^{-5} s^{-1} for both boron-free and boron-containing alloys collected using the *in-situ* module.
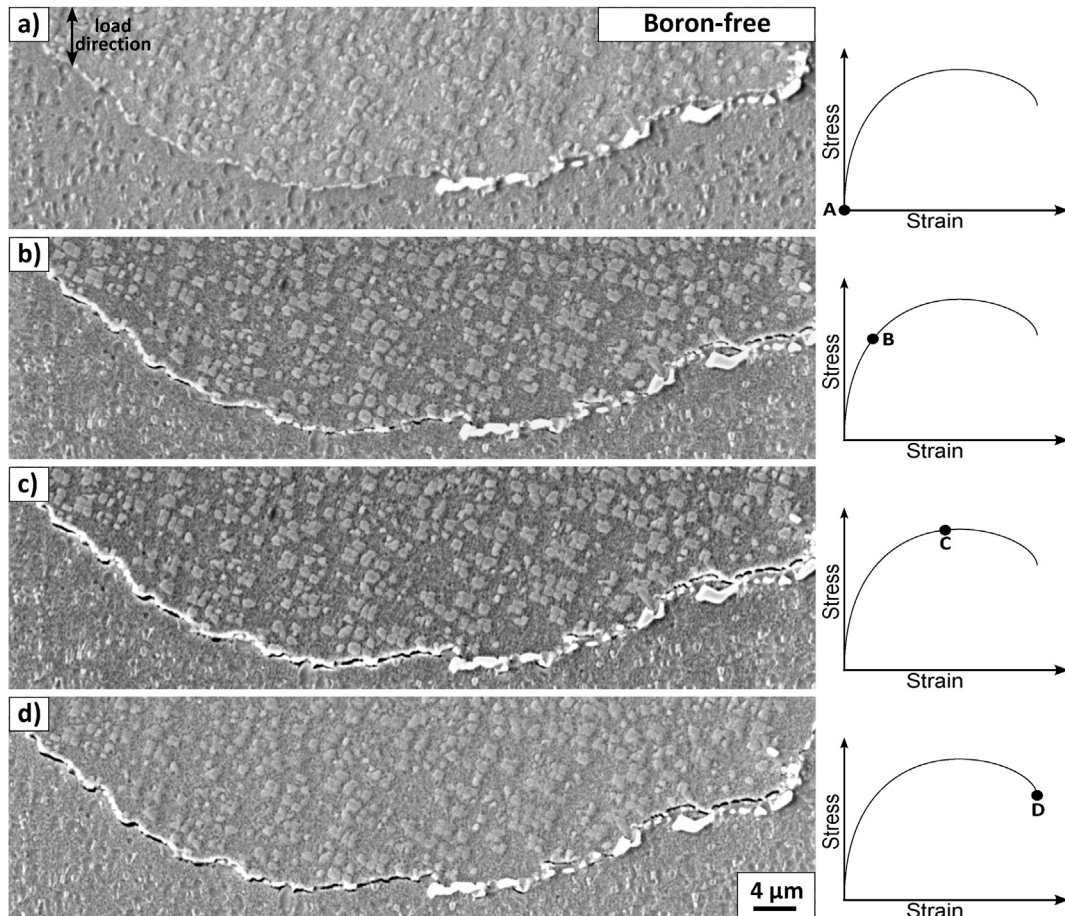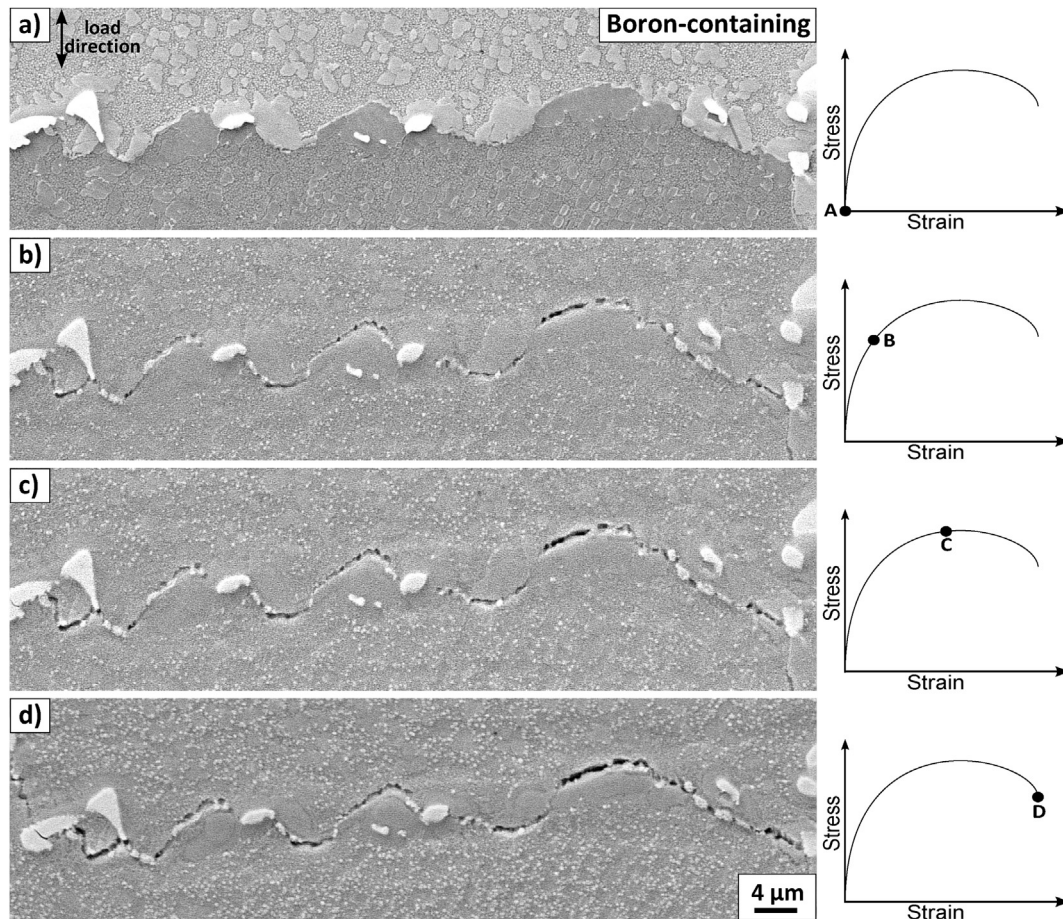
tested in tension to failure at 750 °C and under displacement control with a speed of 0.1 μm s^{-1} using the *in-situ* tensile module. All the figures shown in this study from the *in-situ* investigations were captured at 750 °C. Engineering stress *vs.* engineering strain curves are illustrated in Fig. 9. Although a difference in strain is observed between the *in-situ* and ETMT measurements, the boron-containing alloy performs better in terms of ductility compared to the boron-free variant. A good correlation in the yield point between the ETMT and *in-situ* measurements can be seen.

Figs. 10 and 11 illustrate series of secondary SEM images of fully heat treated grain boundary regions of boron-free and boron-containing alloys tested in tension to failure, respectively. In both cases, damage formation is concentrated solely at the grain boundaries, resulting in intergranular failure. However, differences are observed in the crack propagation along the grain boundaries between the two alloys. In particular, in the boron-free case voids form just after yield (Fig. 10(b)) along the grain boundary. Voids form at incoherent interfaces at the grain boundaries, particularly between the $M_{23}C_6$ and the incoherent grain. As strain is increased, voids grow and interlink leading to a continuous crack path along the grain boundary.

By contrast, in the boron-containing alloy, voids form only at interfaces perpendicular to tensile axis (Fig. 11(b)). As the test proceeds and strains increase, voids coalesce. Due to the serrated character of the grain boundary, this process cannot form a continuous crack path that would lead to premature failure as in the boron-free alloy. Excessive cracking of intergranular MC

segments of the boundary that are perpendicular to the load axis. Boundary segments inclined at ± 45° to the loading axis have relatively low GND density associated with them.

Moreover, boron-free and boron-containing specimens were

Fig. 10. Sequential SEM images of a fully heat treated grain boundary region of the boron-free alloy tested in tension to failure: a) prior to deformation, b) after yield point, c) ~3% strain and d) after failure. Note that the tensile axis is approximately perpendicular to the grain boundary.

Fig. 11. Sequential SEM images of a fully heat treated grain boundary region of the boron-containing alloy tested in tension to failure: a) prior to deformation, b) after yield point, c) ~3% strain and d) after failure. Note that the tensile axis is approximately perpendicular to the grain boundary.

Table 2
Summary of serrated grain boundaries and corresponding misorientation, serration amplitude and wavelength measurements for the boron-containing alloy.

Misorientation theta, deg	Amplitude A, μm	Wavelength λ, μm
26	1.3	4.8
28	1.6	3.1
40	1.2	3.7
40	1.2	3.8
56	1.5	3.3

carbides was not observed at 750 °C for either alloy.

5. Discussion

5.1. The ductilising effect of boron

Our results provide unique insights into the mechanism of ductility improvement, which is more pronounced with boron and at relatively slow strain rates, see Fig. 5. At such conditions, the grain boundary character plays the most important role on the mechanical properties. Void formation and coalescence along the grain boundaries determine that the failure is intergranular.

By contrast, at higher strain rates the ductilising effect of boron is less striking. In this case the failure mechanism is not predominantly controlled by the diffusional phenomena at grain boundaries; instead the γ' volume fraction controls the mechanical properties. This is to b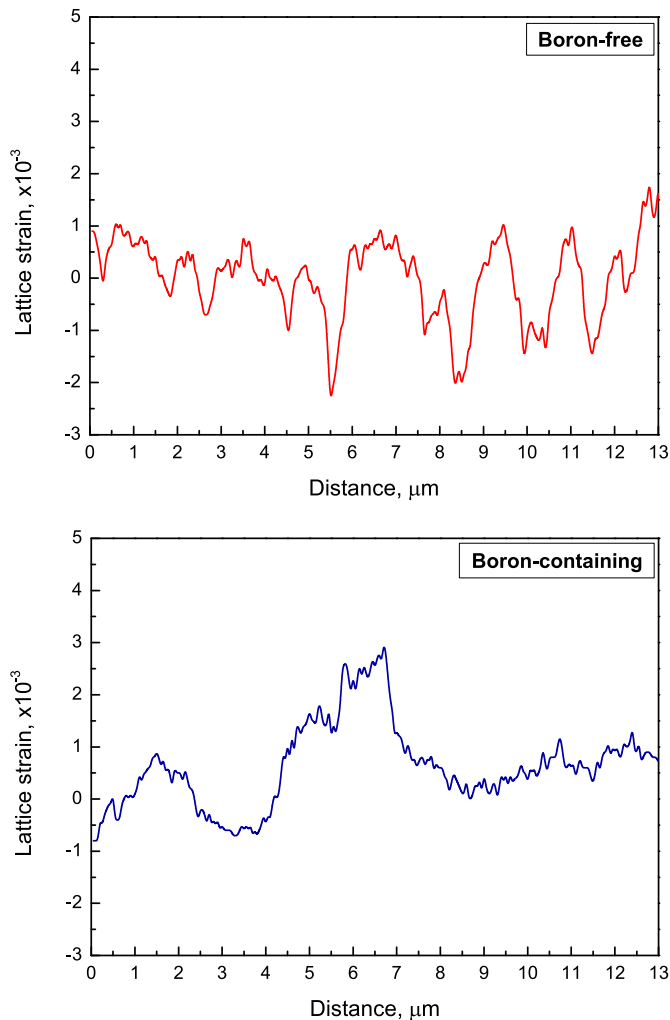e expected as the tensile performance of polycrystalline superalloys is known to be controlled by the γ' volume fraction [4]. In our tests, the volume fraction of γ' particles was not altered by the addition of boron and the γ' forming elements were kept constant between the two alloys. Thus, the performance of the boron-free and boron-containing alloy at higher strain rates was similar.

Moreover, it was shown that the addition of boron results in grain boundary segments being serrated; this effect would appear to play a role in ductility improvement. The misorientation between the grains where serration occurs was measured using the EBSD method. The measured misorientation between the two investigated grains presented in Fig. 3(b) is listed in Table 2 (1st measurement); information from other serrated grain boundaries is also given. In this study serration was observed only for random high angle grain boundaries and not for low angle or special grain boundaries.

Winning *et al.* [31] have shown that high angle grain boundaries can move under the influence of an external shear stress. In a similar manner, increased lattice strain energy caused by the segregation of elements such as boron to the grain boundaries can initiate grain boundary motion which will eventually result in a serrated grain boundary. The segregation needs to be discontinuous in order for different segments of the grain boundary to exhibit a different lattice strain energy.

In Figs. 2(b) and 3(b) the different distribution of lattice strains are evident between the boron-free and boron-containing alloy. In the case of the boron-free alloy, the lattice strains are shown to be uniformly distributed whereas the addition of boron resulted in the

Fig. 12. Lattice strain line-scans across the grains as denoted in Fig. 2(b) and 3(b) for the boron-free and boron-containing, respectively.

serration amplitude and wavelength were measured for the various grain boundaries, indicating that there is no correlation between the misorientation and the magnitude of serration, for the selected boundaries observed in this work.

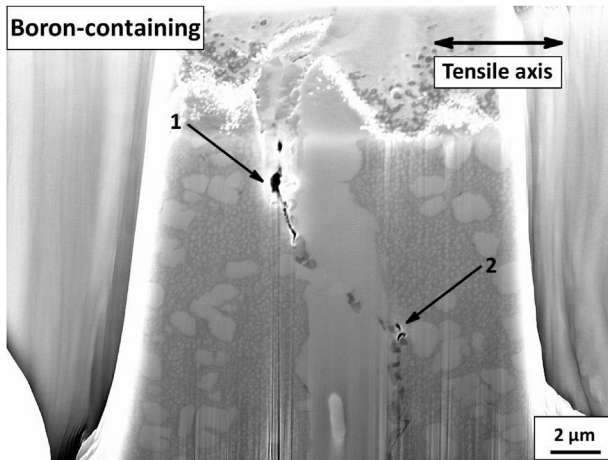### 5.2. Crack initiation and propagation

The EBSD analysis has shown that a transition from planar to serrated grain boundaries can be achieved by the minor addition of boron. Serrated grain boundaries can dramatically improve mechanical properties by retarding crack growth, impeding cavity link and lengthening the propagation path along the grain boundaries [32]. This study adds that at the lowest investigated strain rates, it is evident that voids form at incoherent interfaces along the grain boundaries, as observed in Figs. 10 and 11. At those particular sites, the catastrophic accumulation of stresses at the grain boundary regions leads to intergranular failure.

The HR-EBSD strain maps obtained from the interrupted tensile specimens combined with the observations from the *in-situ* tensile tests were used to identify the crack initiation sites. Although the HR-EBSD analyses were performed at room temperature which could result in the measurement of residual thermal strains during the cooling, regions of high GND density were observed to correlate well with the crack initiation sites observed at 750 °C during the *in-situ* tensile tests. Moreover, the elastic strain distributions after deformation are very different compared to those after the full heat treatment, giving unambiguous evidence that the microstructure has been affected by the deformation. Thus, the resulting lattice strain distributions here cannot be explained by thermal contraction alone.

In the case of the boron-free alloy, voids form at the interfaces of between the $M_{23}C_6$ particles and the γ/γ' microstructure. Due to the planar character of the grain boundary, voids can interlink somewhat more easily, forming a continuous intergranular crack path. By contrast — in the case of the boron-containing alloy — it is more difficult for the voids formed at grain boundaries to interlink. Thus, crack propagation is retarded in the boron-containing case. However, voids were found to initiate between the M_5B_3 borides and the γ/γ' microstructure, when the borides are at the segments of the grain boundary perpendicular to load axis. It is apparent that an optimal volume fraction of borides controlled by the addition of boron is necessary. Beyond that limit boron is rather detrimental for the mechanical properties, as shown in the case of STAL15-CC [3].

Subsurface characterisation of deformed specimens has also been performed to further substantiate the HR-EBSD and microstructure observations made on the surface. The boron-containing specimen was sectioned using a dual column FIB instrument. Fig. 13 illustrates a serrated grain boundary tested at 750 °C and strain rate 2×10^{-5} s^{-1}; note the load axis is in the horizontal direction. It is shown that the crack propagates at the interface perpendicular to tensile axis and its propagation is retarded when it reaches the part of the grain boundary not perpendicular to the tensile axis (arrow 1). A second void can also be seen forming far from the surface of the specimen without interlinking with the main crack (arrow 2). Note that the second void forms at the grain boundary segment perpendicular to tensile axis.

Moreover, it was shown that the addition of boron resulted in the formation of γ' layers at the grain boundaries of the boron-containing alloy. It has been suggested that the formation of γ' envelopes is driven by the reduction of the interfacial energy which was primarily increased by the addition of boron [33,34]. It is known that the interfacial energy can be influenced by the interface orientation and the nature of the segregating element [35]. Thus, the addition of boron may result in the formation of γ' envelopes.

serrated segments of the grain boundary leading to higher lattice strains compared to grain interior.

Fig. 12 shows an arbitrary line-scans across the grains of the boron-free and boron-containing alloys, showing the measured lattice strain as a function of distance. The position of the line-scans in the strain maps is shown in Figs. 2(b) and 3(b). The higher lattice strains at the grain boundary compared to those in the bulk are apparent in the boron-containing alloy. The fluctuation of lattice strains across the grains in the boron-free alloy are present from the secondary γ' precipitates. A fluctuation of similar amplitude and spacing is not observed in the boron-containing alloy, as expected in absence of secondary γ'.

It can be argued that the observed residual elastic strains at room temperature are not representative of the strains during the formation of the serrated boundaries. However, the grain boundary morphology and the γ' layers decorating the grain boundaries is certainly a result of the addition of boron. Thus, the presence of this grain boundary element certainly does influence the spatial distribution of lattice strain. However, the beneficial effect of boron is indirect rather than direct on the mechanical properties, by altering the grain boundary character rather than by directly improving grain boundary cohesion.

The amplitude and wavelength of the serrated grain boundaries were measured and shown in Table 2. Similar values for the

Fig. 13. SEM image of FIB-section of a serrated grain boundary tested at 750 °C and strain rate $2 \times 10^{-5}\,\mathrm{s}^{-1}$. The arrows indicate voids at interfaces perpendicular to tensile axis. Continuous crack path is not observed.

The γ' layers can prevent the accumulation of plastic deformation at the interfaces between MC and γ/γ' microstructure and thus retard crack initiation at these specific sites. This beneficial effect of γ' layers will be more pronounced at temperatures lower than 750 °C, when the MC carbides exhibit low ductility. By contrast, during prolonged exposure to elevated temperature decomposition of MC carbides that are enveloped within a γ' layer would be detrimental to the mechanical properties. More specifically, high amounts of Ta from the decomposed MC carbide would diffuse through the γ' layer leading to a region of high Ta concentration, leading eventually to the formation of the brittle η phase [36]. Such η phase particles can serve as crack initiation sites, thus it is necessary to carefully control the volume fraction of the grain boundary γ' layers.

5.3. Boron vs. carbon as preferred grain boundary element

This work contributes to a growing body of evidence which indicates that boron rather than carbon is the most crucial grain boundary strengthener in nickel-based superalloys. It has been shown that minor additions of boron are beneficial to the mechanical properties by controlling the grain boundary character i.e. suppression of $M_{23}C_6$ carbides and precipitation of M_5B_3 borides and formation of serrated grain boundaries. By contrast, the addition of carbon and the subsequent formation of various carbides (MC, $M_{23}C_6$) and their effect on superalloys still remains controversial [3].

In this study, excessive cracking of MC carbides during the *in-situ* tensile tests to failure at 750 °C was not observed for both alloys. However, these tests last no longer than 2 h, so the long-term stability of MC carbides cannot be completely evaluated. It is well known that MC carbides oxidise faster than the γ/γ' microstructure and surface eruptions occur as a result of the oxidation in flat unstressed specimens [37–39]. Considering these factors, flat polished and unstressed samples from both boron-free and boron-containing alloys were exposed at 750 °C for 50 h.

Our observations are illustrated in Fig. 14(a). MC carbides oxidise causing surface eruptions in the polished unstressed boron-free and boron-containing specimens exposed at 750 °C for 50 h. Such volume expansion can cause locally high stress concentrations to a region with pre-existing strains around MC carbides due to heat treatment, leading eventually to the formation of microcracks. Besides, porosity around the oxidised MC carbide was observed as

shown in Fig. 14(b). It is thus suggested that during over prolonged exposure times, MC carbides can serve as location for crack initiation, particularly when they reside at grain boundaries where diffusion-driven phenomena are present.

Moreover, secondary SEM micrographs of FIB-sections from grain boundary regions revealed γ' denuded zones along the grain boundaries of the boron-free alloy. No $M_{23}C_6$ carbides were found to at least a depth of up to 7 µm as it can be seen in Fig. 15(a). By contrast, in the boron-containing alloy γ' denuded areas were not observed and M_5B_3 were present, as it is illustrated in Fig. 15(b). The occurrence of areas susceptible to early fracture such as the γ' denuded zones is clearly undesirable, particularly when they form during short times at elevated temperature [40]. In addition, first-principle calculation have shown that the Ni/M_5B_3 interfaces are more resistant towards O-embrittlement than coherent Ni/Ni$_3$Al interfaces [41]. It is therefore suggested that the precipitation of borides is more preferable than the precipitation of $M_{23}C_6$ carbides, in order to achieve a more stable microstructure and grain boundary character.

In summary, it is clear that the addition of boron is crucial for nickel superalloys, whilst lower carbon levels — to provide a smaller MC volume fraction — may well lead to improvements in mechanical properties.
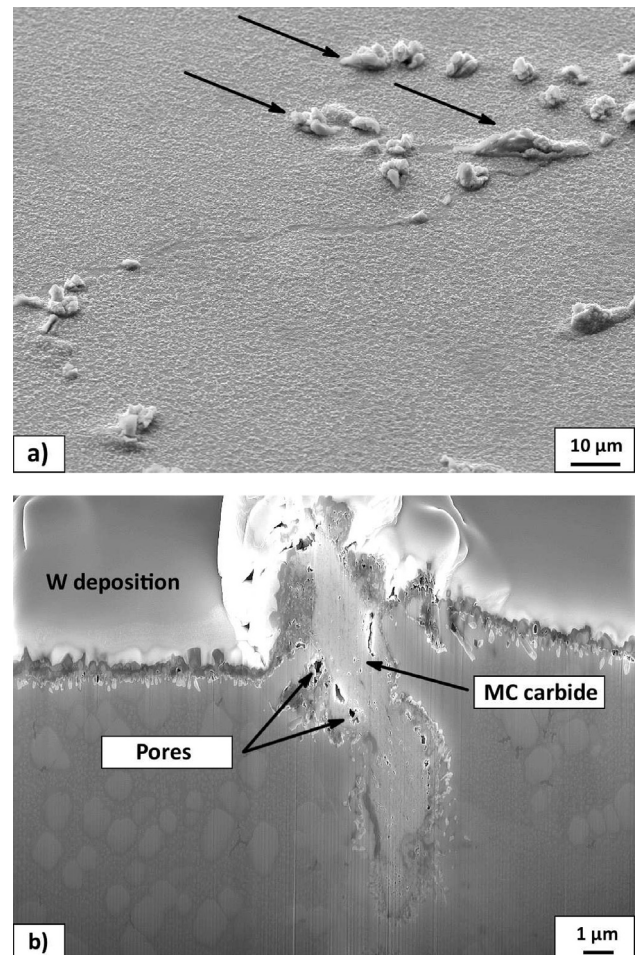
Fig. 14. Secondary SEM images showing: a) surface eruptions due to the oxidation of Ta-rich MC carbides as indicated by the arrows (specimen tilted 54°) and b) FIB-section of oxidised MC carbide from the boron-containing alloy exposed at 750 °C for 50 h. The oxidised carbides were confirmed by energy dispersive X-ray analysis.
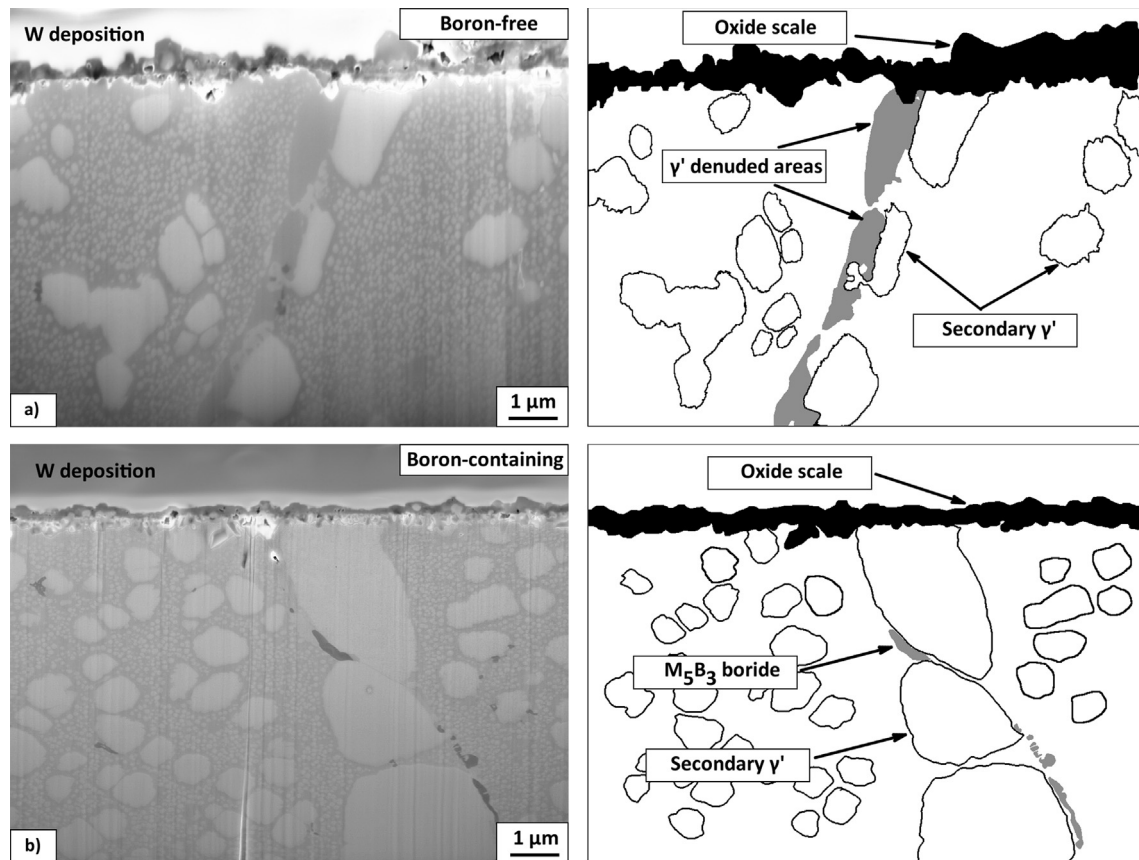
Fig. 15. SEM figures of FIB sections from grain boundary regions of: a) boron-free and b) boron-containing alloy exposed at 750 °C for 50 h, alongside corresponding descriptive schematic illustrations.

6. Conclusions

The mechanical behaviour of a prototype nickel-based super-alloy has been studied at elevated temperature, with emphasis on the improvement in ductility conferred by boron. A miniaturised electro-thermal mechanical testing system and an *in-situ* SEM testing module with complementary HR-EBSD strain mapping analysis have been used. The following specific conclusions have been drawn:

- Addition of boron improves the ductility under tensile stress at 750 °C and at a relatively low strain rate of 2×10^{-5} s^{-1}; no improvement in ductility was observed at higher strain rates.
- Any possible influence of surface effects — for example preferential oxidation at grain boundaries — has been ruled out, by making use of *in-situ* tensile tests under vacuum at 750 °C.
- Characterisation of the grain boundaries with high-resolution EBSD strain mapping revealed localised regions of strain in the vicinity of serrated random high angle grain boundaries, induced indirectly by the presence of boron.
- The role of preferential void formation at segments of grain boundary has been clarified using *in-situ* tensile tests and high-resolution EBSD strain mapping; this effect is profound in the boron-free case but boron addition and thus grain boundary serration retards void formation and cavity propagation.
- The evidence presented indicates that the serration of the grain boundaries induced by boron addition plays a role in the ductility enhancement; however, one cannot eliminate entirely a possible effect of the carbide-to-boride transition.

References

[1] L.H. Rettberg, T.M. Pollock, Localized recrystallization during creep in nickel-based superalloys GTD444 and René N5, Acta Mater. 73 (2014) 287–297.
[2] J.L.W. Carter, M.W. Kuper, M.D. Uchic, M.J. Mills, Characterization of localized deformation near grain boundaries of superalloy René-104 at elevated temperature, Mater. Sci. Eng. A 605 (2014) 127–136.
[3] P. Kontis, H.A. Mohd Yusof, S. Pedrazzini, M. Danaie, K.L. Moore, P.A.J. Bagot, M.P. Moody, C.R.M. Grovenor, R.C. Reed, On the effect of boron on grain boundary character in a new polycrystalline superalloy, Acta Mater. 103 (2016) 688–699.
[4] R.C. Reed, C.M.F. Rae, 22-Physical metallurgy of the Nickel-based Superalloys, in: D.E. Laughlin, K. Hono (Eds.), Physical Metallurgy, fifth ed., Elsevier, Oxford, 2014, pp. 2215–2290.
[5] E.M. Francis, B.M.B. Grant, J.Q. da Fonseca, P.J. Phillips, M.J. Mills, M.R. Daymond, M. Preuss, High-temperature deformation mechanisms in a polycrystalline nickel-base superalloy studied by neutron diffraction and electron microscopy, Acta Mater. 74 (2014) 18–29.
[6] H.U. Hong, H.W. Jeong, I.S. Kim, B.G. Choi, Y.S. Yoo, C.Y. Jo, Significant decrease in interfacial energy of grain boundary through serrated grain boundary transition, Philos. Mag. 92 (2012) 2809–2825.
[7] A.-C. Yeh, K.-W. Lu, C.-M. Kuo, H.-Y. Bor, C.-N. Wei, Effect of serrated grain boundaries on the creep property of Inconel 718 superalloy, Mater. Sci. Eng. A 530 (2011) 525–529.
[8] A. Wisniewski, J. Beddoes, Influence of grain-boundary morphology on creep of a wrought Ni-base superalloy, Mater. Sci. Eng. A 510–511 (2009) 266–272.

[9] H. Hong, I. Kim, B. Choi, M. Kim, C. Jo, The effect of grain boundary serration on creep resistance in a wrought nickel-based superalloy, Mater. Sci. Eng. A 517 (2009) 125–131.

[10] H.L. Danflou, M. Marty, A. Walder, Formation of serrated grain boundaries and their effect on the mechanical properties in a P/M nickel base superalloy, in: S. Antolovich, R. Stusrud, R. MacKay, D. Anton, T. Khan, R. Kissinger, D. Klarstrom (Eds.), Superalloys 1992, The Minerals, Metals and Materials Society, 1992, pp. 63–72.

[11] J.M. Larson, S. Floreen, Metallurgical factors affecting the crack growth resistance of a superalloy, Metall. Trans. A 8 (1977) 51–55.

[12] R.J. Mitchell, H.Y. Li, Z.W. Huang, On the formation of serrated grain boundaries and fan type structures in an advanced polycrystalline nickel-base superalloy, J. Mater. Process. Technol. 209 (2009) 1011–1017.

[13] A.K. Koul, G.H. Gessinger, On the mechanism of serrated grain boundary formation in Ni-based superalloys, Acta Metall. 31 (1983) 1061–1069.

[14] C.L. Qiu, P. Andrews, On the formation of irregular-shaped gamma prime and serrated grain boundaries in a nickel-based superalloy during continuous cooling, Mater. Charact. 76 (2013) 28–34.

[15] H.L. Danflou, M. Macia, T.H. Sanders, T. Khan, Mechanisms of formation of serrated grain boundaries in nickel base superalloys, in: R. Kissinger, D. Deye, D. Anton, D. Cetel, M. Nathal, T. Pollock, D. Woodford (Eds.), Superalloys 1996, The Minerals, Metals and Materials Society, 1996, pp. 119–127.

[16] L. Jiang, R. Hu, H. Kou, J. Li, G. Bai, H. Fu, The effect of $M_{23}C_6$ carbides on the formation of grain boundary serrations in a wrought Ni-based superalloy, Mater. Sci. Eng. A 536 (2012) 37–44.

[17] M.F. Henry, Y.S. Yoo, D.Y. Yoon, J. Choi, The dendritic growth of precipitates and grain, Metallurgical Transactions A 24 (1993) 1733–1743.

[18] Y.S. Lim, D.J. Kim, S.S. Hwang, H.P. Kim, S.W. Kim, $M_{23}C_6$ precipitation behavior and grain boundary serration in Ni-based Alloy 690, Mater. Charact. 96 (2014) 28–39.

[19] D. McLean, Grain Boundaries in Metals, Oxford University Press, London, 1957.

[20] F.H. Latief, H.U. Hong, T. Blanc, I.S. Kim, B.G. Choi, C.Y. Jo, J.H. Lee, Influence of chromium content on microstructure and grain boundary serration formation in a ternary Ni-xCr-0.1C model alloy, Mater. Chem. Phys. 148 (2014) 1194–1201.

[21] L. Letellier, S. Chambreland, P. Duval, D. Blavette, Grain boundary segregation in nickel base superalloys Astroloy: an atom-probe study, Appl. Surf. Sci. 67 (1993) 305–310.

[22] A.J. Wilkinson, G. Meaden, D.J. Dingley, High-resolution elastic strain measurement from electron backscatter diffraction patterns: new levels of sensitivity, Ultramicroscopy 106 (2006) 307–313.

[23] J.F. Nye, Some geometrical relations in dislocated crystals, Acta Metall. 1 (1953) 153–162.

[24] P.D. Littlewood, T.B. Britton, A.J. Wilkinson, Geometrically necessary dislocation density distributions in Ti6Al4V deformed in tension, Acta Mater. 59 (2011) 6489–6500.

[25] J. Jiang, T.B. Britton, A.J. Wilkinson, Evolution of dislocation density distributions in copper during tensile deformation, Acta Mater. 61 (2013) 7227–7239.

[26] J. Jiang, T.B. Britton, A.J. Wilkinson, Mapping type III intragranular residual stress distributions in deformed copper polycrystals, Acta Mater. 61 (2013) 5895–5904.

[27] G. Miyamoto, A. Shibata, T. Maki, T. Furuhara, Precise measurement of strain accommodation in austenite matrix surrounding martensite in ferrous alloys by electron backscatter diffraction analysis, Acta Mater. 57 (2009) 1120–1131.

[28] P.S. Karamched, A.J. Wilkinson, High resolution electron back-scatter diffraction analysis of thermally and mechanically induced strains near carbide inclusions in a superalloy, Acta Mater. 59 (2011) 263–272.

[29] T. Zhang, D.M. Collins, F.P.E. Dunne, B.A. Shollock, Crystal plasticity and high-resolution electron backscatter diffraction analysis of full-field polycrystal Ni superalloy strains and rotations under thermal loading, Acta Mater. 80 (2014) 25–38.

[30] H.W. Gene Simmons, Single Crystal Elastic Constants and Calculated Aggregate Properties, M.I.T. Press, 1970.

[31] M. Winning, G. Gottstein, L.S. Shvindlerman, Migration of grain boundaries under the influence of an external shear stress, Mater. Sci. Eng. A 317 (2001) 17–20.

[32] J.G. Yoon, H.W. Jeong, Y.S. Yoo, H.U. Hong, Influence of initial microstructure on creep deformation behaviors and fracture characteristics of Haynes 230 superalloy at 900 °C, Mater. Charact. 101 (2015) 49–57.

[33] B.C. Yan, J. Zhang, L.H. Lou, Effect of boron additions on the microstructure and transverse properties of a directionally solidified superalloy, Mater. Sci. Eng. A 474 (2008) 39–47.

[34] J. Wang, L. Zhou, L. Sheng, J. Guo, The microstructure evolution and its effect on the mechanical properties of a hot-corrosion resistant Ni-based superalloy during long-term thermal exposure, Mater. Des. 39 (2012) 55–62.

[35] P. Lejček, Grain Boundary Segregation in Metals, Springer, 2010.

[36] X.Z. Qin, J.T. Guo, C. Yuan, C.L. Chen, H.Q. Ye, Effects of long-term thermal exposure on the microstructure and properties of a cast Ni-base superalloy, Metall. Mater. Trans. A 38 (2007) 3014–3022.

[37] J. Litz, A. Rahmel, M. Schorr, Selective carbide oxidation and internal nitridation of the Ni-base superalloys IN738LC and IN939 in air, Oxid. Metals 30 (1988) 95–105.

[38] T. Connolley, P.A.S. Reed, M.J. Starink, Short crack initiation and growth at 600 °C in notched specimens of Inconel 718, Mater. Sci. Eng. A 340 (2003) 139–154.

[39] A. Pineau, D.L. McDowell, E.P. Busso, S.D. Antolovich, Failure of metals II: fatigue, Acta Mater. 107 (2016) 484–507.

[40] R.F. Decker, J.W. Freeman, The Mechanism of Beneficial Effects of Boron and Zirconium on Creep-rupture Properties of a Complex Heat-resistant Alloy, 1960. Transactions of the Metallurgical Society of AIME 218.

[41] S. Sanyal, U.V. Waghmare, T. Hanlon, E.L. Hall, Ni/boride interfaces and environmental embrittlement in Ni-based superalloys: a first-principles study, Mater. Sci. Eng. A 530 (2011) 373–377.